

# Low Profile Pattern-Switchable Multibeam Antenna Consisting of Four L-shaped Microstrip Lines

W. Zhang<sup>1\*</sup>, A. Pal<sup>1</sup>, A. Mehta<sup>1</sup>, D. Mirshekar-Syahkal<sup>2</sup>, H. Nakano<sup>3</sup>

<sup>1</sup> College of Engineering, Swansea University (Bay Campus), Swansea, Wales, SA1 8EN, U.K.

<sup>2</sup> Department of Computing Science and Electronic Engineering, University of Essex, Essex, CO4 3SQ, U.K.

<sup>3</sup> Science and Engineering, Hosei University, Koganei, Tokyo 184-8584, Japan

\*Email: 748451@swansea.ac.uk

**Abstract:** A multibeam antenna consisting of a set of four L-shaped microstrip line sections is presented for pattern switchable applications. A planar electromagnetic band gap substrate is implemented to reduce the antenna profile to  $\lambda_{2.45}/35$ , where  $\lambda_{2.45}$  is the free space wavelength at a design frequency of 2.45 GHz. An impedance matching network is integrated on the lowest layer below a ground plane. The microstrip lines have a resonant frequency of 2.45 GHz and are excited separately. When one of the strips is excited, the antenna generates a tilted beam with a gain of 8.6 dBi. By switching the excitation strip sequentially, a full azimuth beam steering is achieved. When the antenna is located above a large conducting reflector, the antenna maintains its performance. Thus, the antenna is a candidate for moving objects with high speed internet and vehicular tracking.

## 1. Introduction

The pattern switchable function of antennas (arrays) has attracted much attention recently. This function enables the radiation to be pointed in the desired direction. Therefore, it can alleviate adverse effects like co-channel interference [1], multi-path fading and small battery life. In addition, it can extend a network coverage area [2]. Typically, the pattern switchable function is accomplished by phased array antennas [3], where the feeding network of the antenna system contains several radiation elements, several phase shifters, and a signal processor [4]. The phased array antennas are inherently large, lossy, and costly. Multibeam antennas [5- 8] using Butler matrix [9,10] and Rotman lens [5-7] are investigated to reduce the complexity and cost of the feeding network. However, these antenna systems are still large due to multiple antenna elements and they are not suitable for integration in modern portable transceivers.

In contrast, a pattern switchable antenna (PSA) is compact, economically efficient and easy to operate. In recent years, PSAs have been implemented in many communication systems, such as radars [11], wireless local area networks [12], personal communications [13], and satellite communications [14]. Various planar structures have been proposed for realizing PSAs, for instance, the microstrip antennas [15-18], square loop antennas [19-21], and spiral antennas [22-25]. In parallel, electromagnetic band gap (EBG) structures have been investigated for realizing low profile PSAs [26]. Note that in [15-17] pattern switchable function was obtained by employing additional radio frequency (RF) components like PIN diodes which introduce additional complexity in the systems due to their biasing lines. The square loop antennas in [19, 20] require thick substrate height ( $\geq \lambda_g$ , where  $\lambda_g$  is the guided wavelength in the substrate at a design frequency of 2.45 GHz) and in [21] provides a very narrow operating bandwidth. The spiral antennas in [22-25] are suitable for broadband operation. These antennas utilise switches along

the spiral arm to provide beam switching functionality. However, the insertion of switches in the spiral arm causes the polarization randomness from one pattern to another pattern. This eliminates the benefit of beam switchable functionality in a polarisation sensitive communication link.

To overcome this limitation, this study presents a multibeam PSA with a wide range beam tilt tuning function. The antenna is designed for the WiFi frequency band (802.11b/g/n) and has a small height of  $1/23 \lambda_g$ . The antenna can generate four separate tilted beams, where the pattern switchable function is achieved by using a single pole 4 throw RF switch [27], which is controlled by a raspberry Pi [28]. These four beams cover almost  $360^\circ$  in azimuth plane by switching in four different space quadrants. In addition, the antenna also generates multiple patterns, such as, an axial beam, a semi-doughnut beam and a twin-tilted beam by utilising multi-port excitation. A detailed comparison between this work and the similar published works is shown in Table I. This antenna has 12 beams (maximum), great beam tilt ( $35^\circ$ , simulated), high gain (8.6 dBi, simulated) and simple architecture.

Five sections constitute this paper. Section 2 presents the antenna configuration. Section 3 describes the simulated and experimental characteristics of a multibeam PSA. For achieving a wide range beam tilt tuning function, the effects of a large metal reflector, which is underneath the antenna, on the antenna characteristics are also described. The results obtained in this paper is summarized in Section 4.

## 2. Antenna Configuration

Fig. 1 shows the antenna to be discussed in this study: (a) shows the perspective view and exploded perspective view, respectively, (b) the exploded side view, (c) the top view, and (d) the reverse view. The parameters used for Fig. 1 are summarized in Table 2. All substrates are Rogers's

TABLE 1  
COMPARISON BETWEEN SIMILAR WORKS (MEASUREMENT RESULTS)

Parameters.	Selected Operating Frequency (GHz)	GP Width (Square) (mm)	Height (mm)	No. of Beams	Gain (dBi)	Max. Tilt of Each Beam (degree)	Consistent Beams in Four Quadrants	Architecture Main Components
This work	2.45	106.4 ( $\lambda_g/0.75$ )	3.52 ( $\lambda_g/23$ )	12	8.78	33	Yes	L-strips, EBG, Matching-Strips
[10]	12	50 ( $\lambda_g/0.32$ )	1.5 ( $\lambda_g/10.4$ )	9	9.06-10.45	26	No	Radiating-elements, Mutual coupling feeding network
[15]	2.4	100 ( $\lambda_g/0.75$ )	6.4 ( $\lambda_g/11.7$ )	4	5.34	35	Yes	Radiating-elements, Capacitors, PIN Diodes, RF Chokes, Bias Circuit
[16]	2.9	70 ( $\lambda_g/0.98$ )	9.008 ( $\lambda_g/7.62$ )	3	4	28	No	Dipoles, Capacitors, Diodes, RF Chokes, Bias Circuit
[17]	3.5	70 ( $\lambda_g/0.81$ )	3 ( $\lambda_g/19$ )	4	8	31	Yes	Radiating-elements, Capacitors, Inductors, Diodes
[18]	2.4	100 ( $\lambda_g/0.99$ )	1.5 ( $\lambda_g/66$ )	12	5.7-8.2	30	Yes	Patch, Vias

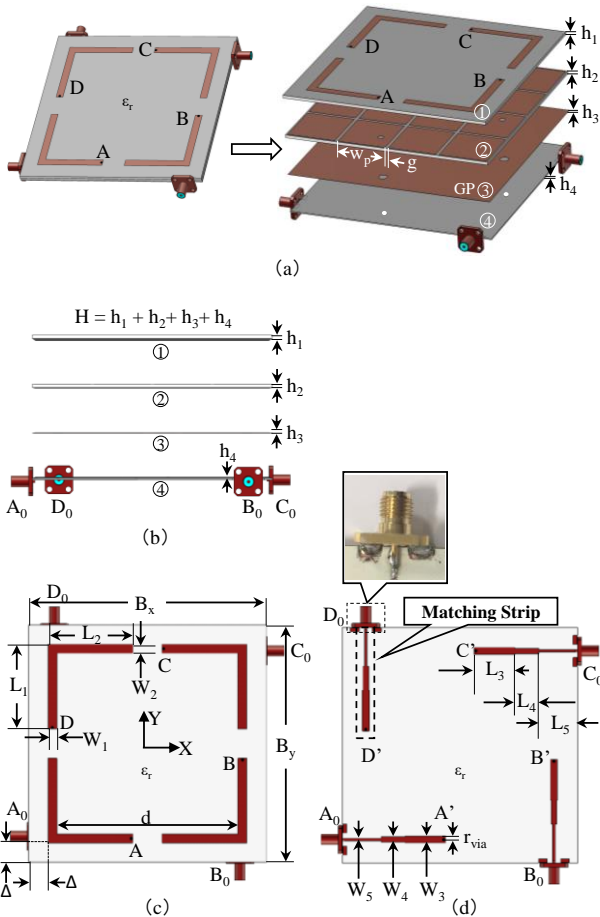


Fig. 1. Antenna structure.

(a) Perspective view, (b) Exploded side view, (c) Top view of layer 1, (d) Reverse view of layer 4.

4350B (relative permittivity,  $\epsilon_r = 3.48$ ; loss tangent,  $\tan \delta = 0.009$ ).

As shown in Figs. 1a and b, the antenna consists of four layers. The first layer 1, which contains the radiation

Table 2 Parameters

Symbol	Value	Symbol	Value
$h_1$	1.5 mm	$\epsilon_r$	3.48
$h_2$	1.5 mm	$W_1$	4 mm
$h_3$	0.02 mm	$W_2$	4 mm
$h_4$	0.5 mm	$W_3$	3.15 mm
H ( $h_1+h_2+h_3+h_4$ )	3.52 mm	$W_4$	2.5 mm
$B_x$	106.4 mm	$W_5$	1.14 mm
$B_y$	106.4 mm	$L_3$	18.31 mm
d	81.1 mm	$L_4$	10.88 mm
$\Delta$	8.65 mm	$L_5$	17.56 mm
$r_{via}$	0.65 mm	$L_1$ (final)	38 mm
$L_1$ (initial)	40.5 mm	$L_2$ (final)	38 mm
$L_2$ (initial)	40.5 mm		

Table 3 EBG Parameters

Symbol	Value	Symbol	Value
$w_p$	26 mm	$g$	0.6 mm
$B_x$	106.4 mm	$B_y$	106.4 mm
$h_2$	1.5 mm		

elements, is placed over an EBG surface (layer 2). The EBG surface is designed to operate at 2.45 GHz. The parameters used for the EBG is shown in Table 3. Below the GP 3, there is a substrate layer 4. Matching circuits are printed on the reverse side of layer 4. The antenna height is  $H = h_1 + h_2 + h_3 + h_4 = 3.52 \text{ mm} = 1/23\lambda_g$ .

Fig. 1c shows that the four identical L-shaped microstrip line sections are printed on a substrate of an area of  $B_x \times B_y = 1.3\lambda_g \times 1.3\lambda_g$  and a thickness (height) of  $h_1$ . The strips are positioned away from the edges of the substrate with

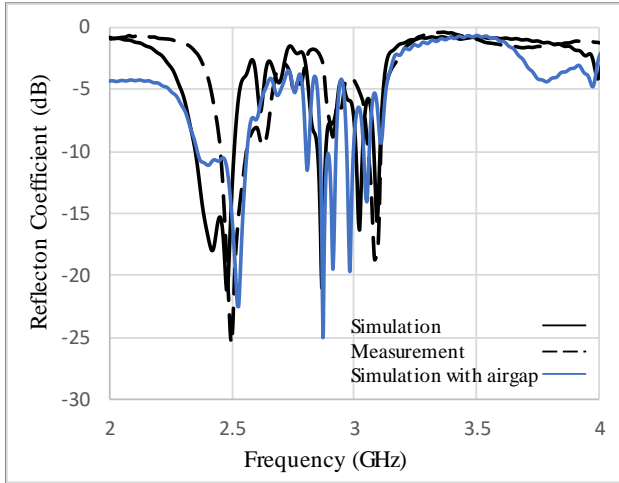
distance  $\Delta$ . The initial dimensions of strip lengths  $L_1$  and  $L_2$  are determined based on the following equation:

$$L = \lambda_g / 2 \quad (1)$$

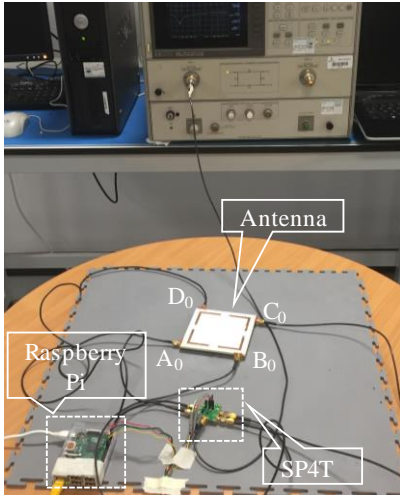
where,

$$\lambda_g = \frac{\lambda_{2.45}}{\sqrt{\frac{1 + \epsilon_r}{2}}} \quad (2)$$

$\lambda_{2.45}$  is the free space wavelength at 2.45 GHz. Later, the  $L_1$  and  $L_2$  are optimized using the CST [29] to obtain better radiation results.



(a)



(b)

**Fig. 2.**  $|S_{11}|$ . (a) Simulation and experimental results (b) Measurement assembly.

The antenna is fed through four SubMiniature version A (SMA) ports. These ports are referred to as  $A_0$ ,  $B_0$ ,  $C_0$  and  $D_0$ . The inner conductor of the SMA port directly interfaces with the first section of a stepped matching transmission line (with width  $W_3$ ), as shown in Fig. 1d. From the end point of  $W_3$ ,  $A'$ , a via (diameter  $2r_{via}$ ) provides the signal path to the

antenna top layer A. Similarly, point  $B'$ ,  $C'$ , and  $D'$  are connected to B, C, and D, respectively. The dimensions of the three-stepped 50- $\Omega$  matching network are shown in Table 2.

### 3. Analysis of the Antenna Characteristics

The simulation results show in this Section are obtained by CST [29].

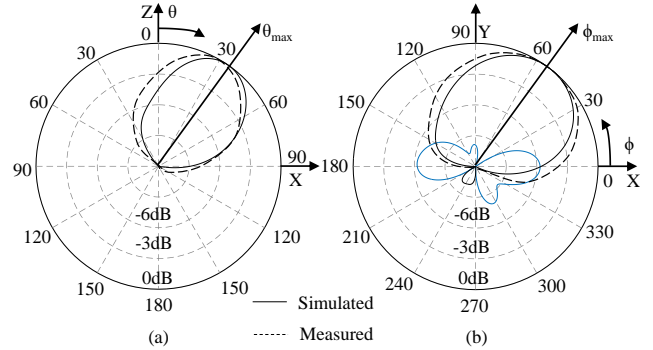


**Fig. 3.** Radiation pattern at 2.45 GHz. (a) In the elevation plane. The maximum beam direction is  $\theta_{max} = 35^\circ$  (simulated) and  $\theta_{max} = 33^\circ$  (measured), (b) In the azimuth plane. The maximum beam direction is  $\phi_{max} = 55^\circ$ .

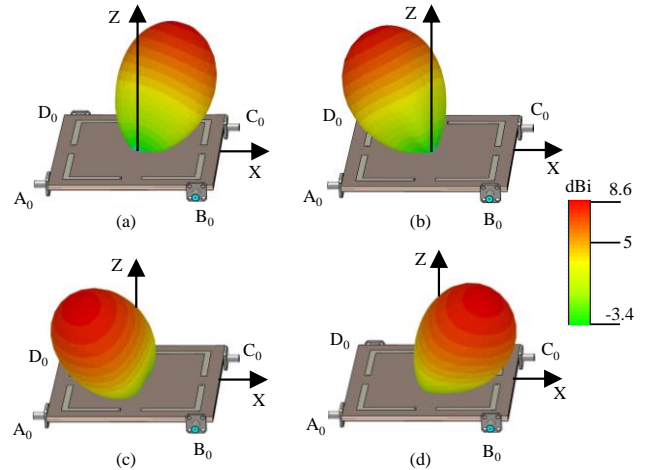


**Fig. 4.** Beam steering at 2.45 GHz. (a)  $A_0$  is excited, (b)  $B_0$  is excited, (c)  $C_0$  is excited, (d)  $D_0$  is excited.

#### 3.1. Input Characteristics

The black solid line in Fig. 2a shows the simulated frequency response of the reflection coefficient ( $|S_{11}|$ ) when port  $A_0$  is excited and the remaining ports  $B_0$ ,  $C_0$ , and  $D_0$  are open circuited. The antenna operates across the 2.45 GHz WiFi frequency band (802.11b/g/n). Fig. 2b shows the antenna measurement setup. Four ports of the antenna are connected to the switch using four semi-rigid cables, each having a length of 30 cm. The switch has an insertion loss of 0.7 dB. Note that each port of the switch is terminated to 50  $\Omega$  when it is under ‘off’ condition. However, since the mutual coupling among the four ports of the antenna is  $< -20$  dB, the effect of the passive port termination on the reflection coefficient is negligible. The measured  $|S_{11}|$  is shown by the dashed line in Fig. 2a. It is found that there are small

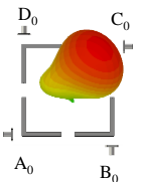
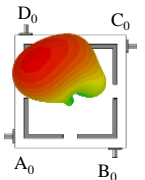
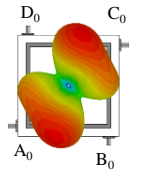
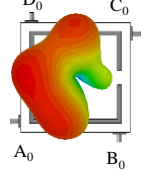
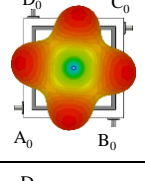
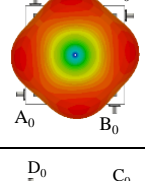
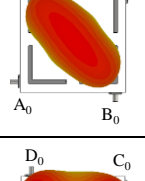
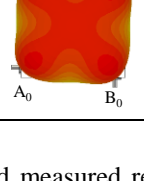
Case	ex: excited op: open-circuited				Beam	Tot. Effic (%)	Gain (dBi)
	A <sub>0</sub>	B <sub>0</sub>	C <sub>0</sub>	D <sub>0</sub>			
I	ex	op	op	op		89.3	8.61
II	ex	ex	op	op		90.8	8.3
III	ex	op	ex	op		74.9	6.72
IV	ex	ex	ex	op		86	6.92
V	ex 0°	ex 0°	ex 0°	ex 0°		89.3	5.99
VI	ex 0°	ex 180°	ex 0°	ex 180°		50	4.95
VII	ex 0°	ex 0°	ex 180°	ex 180°		89.6	7.08
VIII	ex 0°	ex 90°	ex 180°	ex 270°		89	4.42

Fig.5 Multiport Excitation.

differences between simulated and measured results due to fabrication errors. There is a small air (gap) between the GP and the substrate (layer 4). This influences the measurement results and causes a shift from the simulated results. The blue solid line in Fig. 2a shows the simulated  $|S_{11}|$  of the antenna

with a 0.5 mm air (gap) between the GP and layer 4, showing good agreement with the measured results. Note that the same reflection coefficient is reproduced when port B<sub>0</sub>, C<sub>0</sub>, or D<sub>0</sub> is excited, because the antenna is symmetric with respect to the antenna center point.

### 3.2. Radiation Pattern

Fig. 3 shows the radiation pattern at 2.45 GHz, where port A<sub>0</sub> is excited and the remaining ports B<sub>0</sub>, C<sub>0</sub>, and D<sub>0</sub> are kept passive. The antenna generates a radiation beam tilted in the ( $\theta_{\max} = 33^\circ$ ,  $\phi_{\max} = 55^\circ$ ) direction for the measurement versus ( $\theta_{\max} = 35^\circ$ ,  $\phi_{\max} = 55^\circ$ ) direction for the simulation. The antenna provides a measured gain of 8.78 dBi (8.61 dBi for the simulation) in the direction of maximum radiation. The tilted beam is linearly polarised, and the cross polarised component is very small:  $E_\phi \leq -50$  dB, and not visible in the elevation plane. The measured beam has a half-power beam-width of  $\sim 60^\circ$  in the elevation plane ( $\sim 55^\circ$  for the simulation) and  $\sim 100^\circ$  in the azimuth plane ( $\sim 80^\circ$  for the simulation). Thus, the antenna covers an azimuth quadrant of  $0^\circ < \phi_{\max} < 90^\circ$ . The antenna is symmetric with respect to the center point. Therefore, by exciting A<sub>0</sub>, B<sub>0</sub>, C<sub>0</sub>, or D<sub>0</sub> individually (sequentially), the antenna can steer a linearly polarised tilted beam ( $\theta_{\max} = 35^\circ$ ) in four quadrants of ( $\phi_{\max} = 55^\circ$ ,  $\phi_{\max} = 145^\circ$ ,  $\phi_{\max} = 235^\circ$  and  $\phi_{\max} = 325^\circ$ ), as shown in Fig. 4.

### 3.3. Multiport Excitation

In this subsection, it is demonstrated that the antenna can also provide multiple beams by using multiport feeding/excitation. The performance of the antenna with multiport excitation are summarized in Fig.5. Case I, already discussed in sections 3.1 and 3.2, has the highest gain of 8.6 dBi. Case II also presents a high gain of  $>8$  dBi. In Case III, the radiation beam splits into two lobes, resulting in a reduced gain. Note that, the beam is distorted in Case IV. Simultaneous four-port feeding from Case V to Case VIII with different phases is investigated. Different kinds of radiation beams are obtained: semi-doughnut beam, fan axial beam, and axial beam. Case VIII has the lowest gain due to the omnidirectional beam. The beams shown in this Fig. 5 are all linearly polarized, except for Case VIII, which is circularly polarized. Note that these results are only simulated results, and the prototype of a feeding network is not provided for the brevity of the paper; the feeding network is provided in the appendix.

### 3.4. The effect of a large metal reflector on radiation characteristics

The antenna is designed for the intended applications in vehicles or sorting robots. In these applications, the antenna is required to be placed over a large metal reflector. In this subsection the effects of a metal reflector on the antenna characteristics are presented. The GP in the previous sections has an area  $B_x \times B_y$ . In this section, a metal reflector GP' is placed below the layer 4, as shown in Fig. 6. The area of GP' is denoted as  $GP'_x \times GP'_y$ , where  $GP'_x = GP'_y$  (square). There is a gap  $\Delta g$  between layer 4 and the reflector.

Fig. 7 shows the variation of the beam direction and the gain when area ( $GP'_x \times GP'_y$ ) of the reflector is changed, with a fixed gap of  $\Delta g = 0.057\lambda_{2.45}$ . The tilt angle increases as

$GP'_x$  is increased; from  $\theta_{max} = 35^\circ$  to  $\theta_{max} = 65^\circ$ , when reflector's size is increased from  $GP'_x \times GP'_y = 0.82\lambda_{2.45} \times 0.82\lambda_{2.45}$  to  $GP'_x \times GP'_y = 16.4\lambda_{2.45} \times 16.4\lambda_{2.45}$ . The gain almost remains constant:  $\sim 8.5$  dBi across this  $GP'_x$  range.

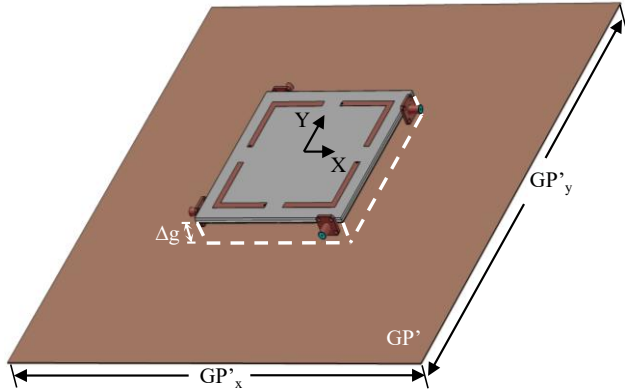


Fig. 6. Metal reflector below layer 4.

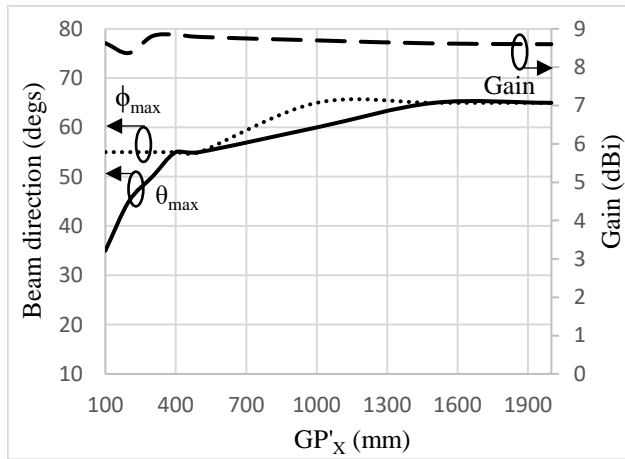


Fig. 7. Variation of gain and main beam direction as a function of side dimension  $GP'_x$  at 2.45 GHz, where  $\Delta g = 0.057\lambda_{2.45}$ .

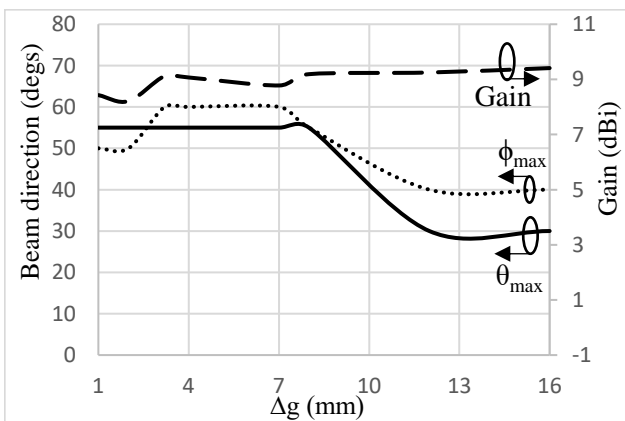
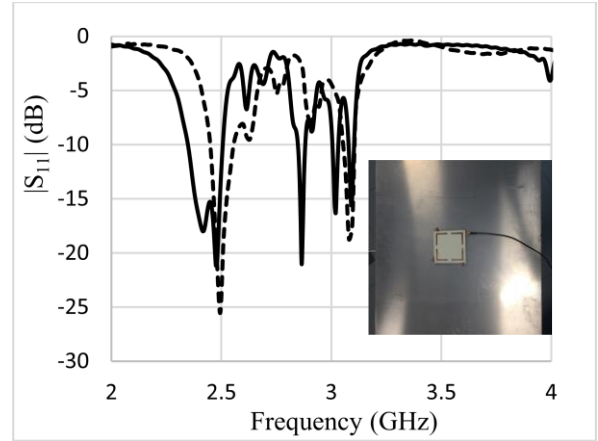


Fig. 8. Gain and beam direction as a function of  $\Delta g$  at 2.45 GHz.

Based on the abovementioned results, a representative reflector size,  $GP'_x = 500$  mm  $= 4.1\lambda_{2.45}$ , is chosen for the following discussion on effects of  $\Delta g$ . It is found from Fig. 8 that, when  $\Delta g$  is less than 8 mm ( $0.066\lambda_{2.45}$ ), the tilt angle is

constant at  $\theta_{max} = 55^\circ$ . However, as the  $\Delta g$  is increased to 16 mm ( $0.13\lambda_{2.45}$ ),  $\theta_{max}$  significantly decreases to  $\theta_{max} = 30^\circ$ . Note that the gain is  $\sim 9$  dBi across a range of 4 mm ( $0.03\lambda_{2.45}$ )  $< \Delta g < 16$  mm ( $0.13\lambda_{2.45}$ ).



Simulation with a reflector ———  
Measurement with a reflector - - - -

Fig. 9.  $|S_{11}|$  for the antenna with a metal reflector ( $GP'_x \times GP'_y = 500$  mm  $\times$  500 mm  $= 4\lambda_{2.45} \times 4\lambda_{2.45}$ ).

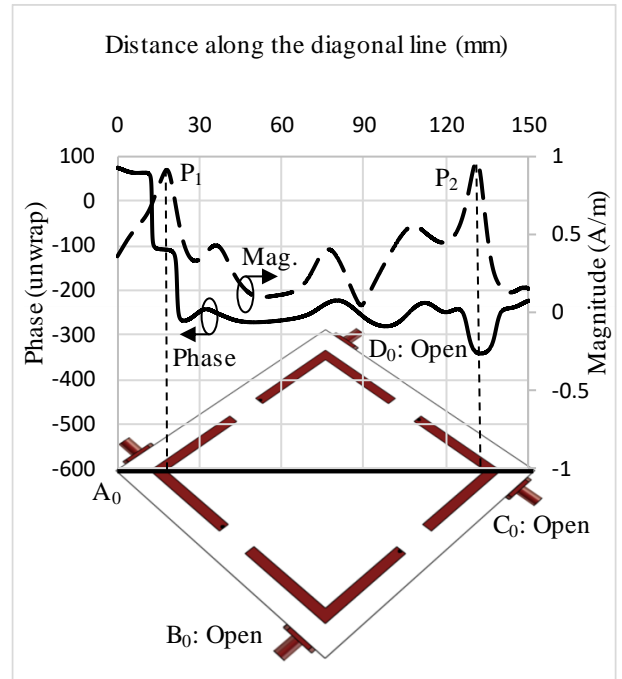


Fig. 10. Phase and magnitude of  $H$ -field in the absence of a reflector.

Fig. 9 shows the reflection coefficient  $|S_{11}|$  with a reflector. The simulation result is confirmed by measured result. Fig. 10 (without a reflector) and Fig. 11 (with a reflector, here we chose the maximum beam tilt, where  $\Delta g = 7$  mm  $= 0.057\lambda_{2.45}$ ,  $GP'_x = 2$  m  $= 16.4\lambda_{2.45}$ , as shown in Fig. 7) show the simulated magnitude and phase of the  $H$ -field in the diagonal direction from the fed port  $A_0$  to the opposite port  $C_0$ . As shown in Figs. 10 and 11, there are two main radiating points (first and second highest magnitudes) along this direction. Focusing on these two radiating points, array

theory is applied for estimating the beam tilt angle. As shown in Fig. 10, the phases at the main radiating points  $P_1$  and  $P_2$  are, respectively,  $-113^\circ$  and  $-336^\circ$ . This provides a  $42^\circ$  tilt angle, which approximates a tilt angle of  $35^\circ$  for the full wave analysis (CST [29]). On the other hand, the phases at the main radiating points in Fig. 11 are  $251^\circ$  and  $29^\circ$ , resulting in a  $58^\circ$  tilt angle, which is close to the full wave analysis result of  $65^\circ$ .

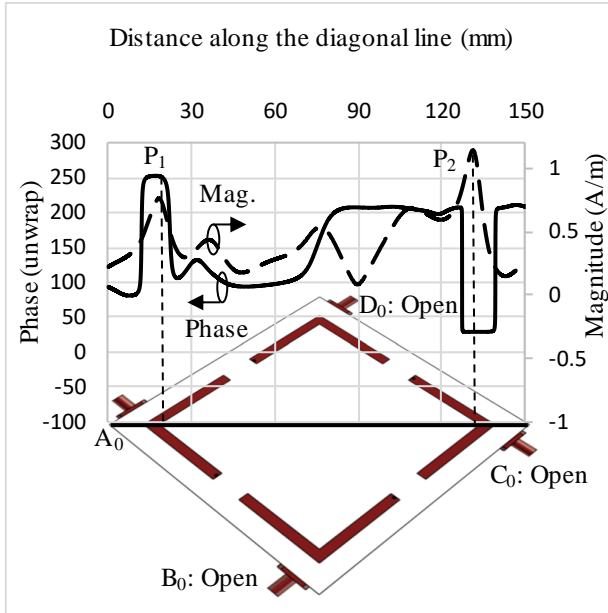


Fig. 11. Phase and magnitude of H-field with a reflector.

This subsection has demonstrated that the gap  $\Delta g$  controls a beam direction ( $\theta_{\max}$ ,  $\phi_{\max}$ ). The gain is almost stable ( $\sim 9$  dBi) and  $|S_{11}|$  is also reasonable ( $< -15$  dB at 2.45 GHz). The beam can be directed toward a base station (beam tilt tuning) using data presented in this section. The beam direction in the azimuth plane is controlled by selecting excitation ports ( $A_0$ ,  $B_0$ ,  $C_0$ ,  $D_0$ ), while the beam direction in the elevation plane is controlled by selecting gap  $\Delta g$ . This is of special importance when moving objects (for example, logistics boxes and vehicles) are driven in weak electromagnetic environment.

#### 4. Conclusions

A four-layer low profile ( $\lambda_{2.45}/35$ ) pattern reconfigurable antenna system composed of four L-shaped microstrip lines has been presented. The antenna utilizes a planar EBG surface for realizing a low-profile structure and has a stepped transmission line impedance matching network, which is integrated on the reverse side of the fourth layer. The length of these L-shaped strips determines the antenna resonant frequency. In this paper, the antenna has been designed for a 2.45 GHz WiFi frequency band (802.11b/g/n). When one of the four strips is excited and the remaining strips are open-circuited, the antenna provides a tilted beam with a gain of 8.6 dBi. The beam is directed in the diagonal direction. A full azimuth beam steering can be achieved by sequentially exciting the L-shaped elements. Further investigation reveals that, when a large flat metal reflector (500 mm  $\times$  500 mm) is placed below the antenna, a wide range of beam tuning ( $\theta_{\max}$  from  $30^\circ$  to  $55^\circ$ ) is obtained with a gain  $> 8$  dBi.

#### 5. References

- [1] Desautel E., Kim D., Kenney J. S. and Kiesling D.: 'Interference mitigation in WLAN networks using client based smart antennas'. Radio and Wireless Conf., Boston, MA, USA, Aug. 2002, pp. 63-66
- [2] Beach M., McGeehan J., Simmonds C., Howard P., Darwood P., Tsoulos G., Nix A., Hafezi P. and Sun Y.: 'European Smart antenna test-beds', J. Commun. Netw., 2000, 2, (4), pp. 317-324
- [3] Pal A., Mehta A., Mirshekar-Syahkal D. and Nakano H.: '2  $\times$  2 phased array consisting of square loop antennas for high gain wide angle scanning With Low Grating Lobes', IEEE Trans. Antennas Propag., Feb 2017., 65, (2), pp. 576-583
- [4] Pozar D.: 'Finite phased arrays of rectangular microstrip patches', IEEE Trans. Antennas Propag., May 1986., 34, (5), pp. 658-665
- [5] Amin D., Omid M., Mohammad Ali S., Parisa D., and Ahad T.: 'Ultra-wideband scanning antenna array with rotman lens', IEEE Trans. Microw. Theory Techn., Sep. 2017., 65, (9), pp. 3435-3442
- [6] Karim T., Mauro E., Laurent Le C., and Ronan S.: 'Multibeam SIW slotted waveguide antenna system fed by a compact dual-layer rotman lens', IEEE Trans. Antennas and Propag., Feb. 2016., 64, (2), pp. 504-514
- [7] Christie S., Cahill R., Mitchell N., Munro Y. and Manabe A.: 'Electronically scanned rotman lens antenna with liquid crystal phase shifters', Electron. Letts., Apr. 2013., 49, (7), pp. 445-447
- [8] Dongfang G., Yingsong Z., Zuping Q., Yujian L., Muftah A. and Can D.: 'A novel 2-D multibeam antenna without beamforming network', IEEE Trans. Antennas and Propag., Jul. 2016., 64, (7), pp. 3177-3180
- [9] Le-Hao Z., Yong-Ling B., Ji-Wei L., Qing-Ling Y., Jinhong G., and Zhe-Feng Y.: 'Miniaturized SIW multibeam antenna array fed by dual-layer 8  $\times$  8 butler matrix', IEEE Antennas Wireless Propag. Lett., 2017, 16, pp. 3018-3021
- [10] Krzysztof W., Kamil S., and Slawomir G.: 'Broadband multibeam antenna arrays fed by frequency-dependent butler matrices', IEEE Trans. Antennas and Propag., Sep. 2017., 65, (9), pp. 4539-4547
- [11] Di Palma L., Clemente A., Dussopt L., Sauleau R., Potier P. and Pouliguen P.: 'Radiation pattern synthesis for monopulse radar applications with a reconfigurable transmitarray antenna', IEEE Trans. Antennas Propag., Sep. 2016., 64, (9), pp. 4148-4154
- [12] Nor M.Z.M., Rahim S.K.A., Sabran M.I., Soh P. J., and Vandenbosch G.A.E.: 'Dual-band, switched-beam, reconfigurable antenna for WLAN applications', IEEE Antennas Wireless Propag. Lett., 2013., 12, pp.1500-1503
- [13] Cao Y., W. Cheung S. and I. Yuk. T.: 'A simple planar polarization reconfigurable monopole antenna for GNSS/PCS', IEEE Trans. Antennas Propag., Feb. 2015., 63, (2), pp. 500-507
- [14] Mitsumoto H., Murata T., Takano K., Fujita M., Tanaka S., Itoh S., Shogen K., Toyama N. and Miyazawa H.: 'A mobile satellite news gathering

system using a flat antenna', IEEE Trans. Broadcasting., Sep. 1996., 42, (3), pp. 272-277

[15] Alam M. and Abbosh A.: 'Beam-steerable planar antenna using circular disc and four PIN-controlled tapered stubs for WiMAX and WLAN applications', IEEE Antennas Wireless Propag. Lett., 2016., 15, pp. 980-983

[16] Bai Y., Xiao S., Liu C., Shuai X. and Wang B.: 'Design of pattern reconfigurable antennas based on a two-element dipole array model', IEEE Trans. Antennas Propag., Sep. 2013., 61, (9), pp. 4867-4871

[17] Shi S. and Ding W.: 'Radiation pattern reconfigurable microstrip antenna for WiMAX application', Electron. Letts., 2015., 51, (9), pp. 662-664

[18] Pal A., Mehta A., Mirshekar-Syahkal D. and Nakano H.: 'A twelve-beam steering low-profile patch antenna with shorting vias for vehicular applications', IEEE Trans. Antennas Propag., Aug. 2017., 65, (8), pp. 3905-3912

[19] Mehta A. and Mirshekar-Syahkal D.: 'Pattern steerable square loop antenna', Electron. Letts., Apr. 2007., 43, (9), pp. 491-493

[20] Pal A., Mehta A., Mirshekar-Syahkal D. and J. Massey P.: 'Short-circuited feed terminations on beam steering square loop antennas', Electron. Letts., Nov. 2008., 44, (24), pp. 1389-1390

[21] Pal A., Mehta A., Mirshekar-Syahkal D. and Nakano H.: 'Low-profile steerable loop antenna with capacitively coupled feeds'. IEEE Antennas Wireless Propag. Lett., 2012., 11, pp. 873-876

[22] Mehta A. and Mirshekar-Syahkal D.: 'Spiral antenna with adaptive radiation pattern under electronic control', IEEE Int. Symp. on Antennas and Propag., Monterey, CA, USA, Jun. 2004, pp. 843-846

[23] Mehta A., Mirshekar-Syahkal D. and Nakano H.: 'Beam adaptive single arm rectangular spiral antenna with switches', IEE Proc-Microw. Antennas Propag., Feb. 2006., 153, (1), pp. 13-18

[24] Jung, C.W., Lee, M.J., Li, G.P., and De Flaviis.: 'Reconfigurable scan-beam single-arm spiral antenna integrated with RF-MEMS switches', IEEE Trans. Antennas and Propag., Feb. 2006., 54, (2), pp. 455-463

[25] Huff G. H. and Bernhard J. T.: 'Integration of packaged RF MEMS switches with radiation pattern reconfigurable square spiral microstrip antennas', IEEE Trans. Antennas and Propag., Feb. 2006., 54, (2), pp. 464-469

[26] Deo P., Mehta A., Mirshekar-Syahkal D., Messy P. J. and Nakano H.: 'Thickness reduction and performance enhancement of steerable square loop antenna using hybrid high impedance surface', IEEE Trans. Antennas and Propag., May. 2010., 58, (5), pp. 1477-1485

[27] 'Analog Devices SP4T Switch HMC241LP3', <http://www.analog.com/media/en/technical-documentation/data-sheets/hmc241lp3.pdf>

[28] 'Raspberry Pi 2 Model B', <https://www.raspberrypi.org/products/raspberry-pi-2-model-b>

[29] 'CST', <https://www.cst.com>.

[30] <http://www.analog.com/media/en/technical-documentation/data-sheets/hmc550.pdf>.

[31] <http://www.psemi.com/pdf/datasheets/pe44820ds.pdf>.

## 6. Appendix

### 6.1. Feeding network for multiport excitation

Fig. 12 shows the schematic diagram of the feeding network for multiport excitation. The feeding network is composed of 1:4 power divider/combiner, four phase shifters

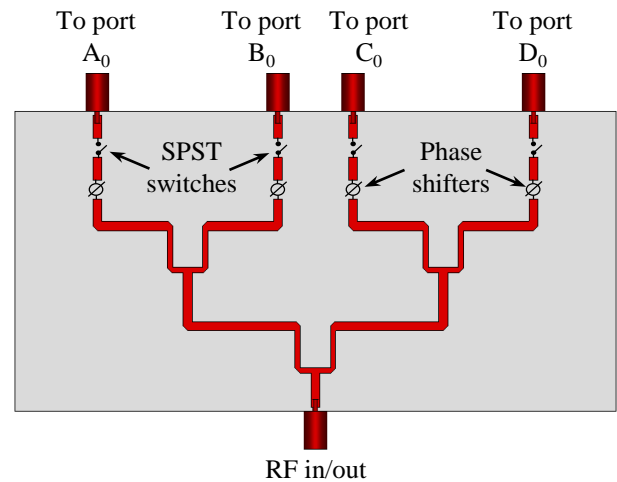


**Fig. 12. Schematic of the feeding network for multiport excitation.**

and four single pole single throw switches (SPST). The feeding network is designed on a Rogers 4350B substrate having a height of 0.5 mm. A GaAs monolithic microwave integrated circuit based SPST failsafe switch [30] is used for achieving the open-circuited condition for the ports. the makes O-state. Four 8-bit digital phase shifters [31] is used to provide the appropriate phases for realizing the multibeam as discussed in Section 3.3.